LETTERS

Spreading rate dependence of gravity anomalies along oceanic transform faults

Patricia M. Gregg[1], Jian Lin[2], Mark D. Behn[2] & Laurent G. J. Montési[2]

Mid-ocean ridge morphology and crustal accretion are known to depend on the spreading rate of the ridge. Slow-spreading mid-ocean-ridge segments exhibit significant crustal thinning towards transform and non-transform offsets[1–12], which is thought to arise from a three-dimensional process of buoyant mantle upwelling and melt migration focused beneath the centres of ridge segments[1,2,4–7,9,10,12]. In contrast, fast-spreading mid-ocean ridges are characterized by smaller, segment-scale variations in crustal thickness, which reflect more uniform mantle upwelling beneath the ridge axis[13–15]. Here we present a systematic study of the residual mantle Bouguer gravity anomaly of 19 oceanic transform faults that reveals a strong correlation between gravity signature and spreading rate. Previous studies have shown that slow-slipping transform faults are marked by more positive gravity anomalies than their adjacent ridge segments[1,2,4,6], but our analysis reveals that intermediate and fast-slipping transform faults exhibit more negative gravity anomalies than their adjacent ridge segments. This finding indicates that there is a mass deficit at intermediate- and fast-slipping transform faults, which could reflect increased rock porosity, serpentinization of mantle peridotite, and/or crustal thickening. The most negative anomalies correspond to topographic highs flanking the transform faults, rather than to transform troughs (where deformation is probably focused and porosity and alteration are expected to be greatest), indicating that crustal thickening could be an important contributor to the negative gravity anomalies observed. This finding in turn suggests that three-dimensional magma accretion may occur near intermediate- and fast-slipping transform faults.

We analyse the residual mantle Bouguer gravity anomaly (RMBA) from 19 oceanic transform fault systems and their adjacent ridge segments at ultraslow- to fast-spreading mid-ocean ridges (Supplementary Fig. 1) with fault slip rates of 1.3–14.5 cm yr^{-1} and fault lengths of 70–350 km (see Methods). RMBA is used to infer local density variations relative to a reference model that includes a 6-km-thick crust. A negative RMBA indicates a mass deficit, which can be due to thickened crust, increased porosity, and/or serpentinized mantle. Conversely, a positive RMBA typically implies crustal thinning. Our results reveal a systematic disparity in the gravity signature between ultraslow-/slow-slipping transform faults and intermediate-/fast-slipping transform faults.

To illustrate these differences, we compare the RMBA at the fast-slipping Siqueiros transform to the RMBA at the slow-slipping Atlantis transform (Fig. 1). The 150-km-long Siqueiros transform located at ~8.3° N on the East Pacific Rise is slipping at ~11.8 cm yr^{-1} and includes five fault segments connected by four intra-transform spreading centres[16] (Fig. 1a). The ridge segments to the north and south of Siqueiros are typical of fast-spreading ridges with axial highs as shallow as 2.0–2.8 km. The ridge transform intersections bounding Siqueiros display overshooting ridge tips[16] typical of ridge transform intersections at magmatically robust ridge segments (Supplementary Figs 2–5). In contrast, the 70-km-long Atlantis transform at 30° N on the Mid-Atlantic Ridge is slipping at ~2.4 cm yr^{-1} and contains a single strike–slip fault zone (Fig. 1b). The ridge segments adjacent to the Atlantis transform display slow-spreading rift valleys and a wide range of axial depths.

As seen in previous gravity studies of the Atlantis transform[2,7,17], more negative RMBA is associated with adjacent ridge segment centres (up to ~80 mGal less than the transform offset), whereas the most positive RMBA is located in the transform fault and fracture zone (Fig. 1d). In contrast, at Siqueiros more positive RMBA is observed along the adjacent ridge segments and more negative values are found within the transform fault and fracture zone domains (up to ~40 mGal less than the adjacent ridge segments). RMBA minimums often correspond to bathymetric highs along the eastern and southern flanks of the fault (Fig. 1c).

The difference in the average RMBA values between transform fault domains and their adjacent ridge segments—$\Delta RMBA_{T-R}$—varies systematically with spreading rate for the 19 transform faults included in this study (Fig. 2, see Methods section for $\Delta RMBA_{T-R}$ calculation). $\Delta RMBA_{T-R} > 0$ implies more positive RMBA along the transform fault domain than along the adjacent ridge segments, whereas $\Delta RMBA_{T-R} < 0$ implies more negative values within the transform fault domain. Along ultraslow- and slow-spreading ridges, the average RMBA in transform fault domains is systematically more positive than along the adjacent ridge segments with $\Delta RMBA_{T-R}$ of up to 45 mGal. However, for spreading rates exceeding ~5 cm yr^{-1} the average RMBA within transform fault domains becomes more negative than on the adjacent ridge segments. Most intermediate- and fast-slipping transforms are associated with $\Delta RMBA_{T-R}$ of −4 to −14 mGal, whereas the Blanco transform is associated with a $\Delta RMBA_{T-R}$ of −40 mGal (Fig. 2 and Supplementary Table 1).

Previous studies attribute positive RMBA along slow-slipping transform faults to decreased crustal accretion towards the end of ridge segments and therefore crustal thinning within the transform fault domain[1,2,4,6]. If the negative RMBA observed at intermediate- and fast-slipping transforms also reflects variations in crustal thickness, these anomalies indicate crustal thickening within the transform domain. However, negative RMBA can also arise from other factors, such as cracking and alteration at transform fault offsets[5,8–10]. Therefore, we use two-dimensional (2D) gravity models to estimate the amplitude of $\Delta RMBA_{T-R}$ corresponding to: (1) increased rock porosity; (2) serpentinization of mantle peridotite; and (3) crustal thickening (Fig. 3, Supplementary Fig. 7, and Supplementary Methods).

Low seismic velocities recorded in the Clipperton transform and near the Siqueiros transform have been attributed to increased cracking and porosity within the transform domain[15,18]. The observed

[1]Department of Geology and Geophysics, Massachusetts Institute of Technology/Woods Hole Oceanographic Institution Joint Program, [2]Department of Geology and Geophysics, Woods Hole Oceanographic Institution, Woods Hole, Massachusetts 02543, USA.

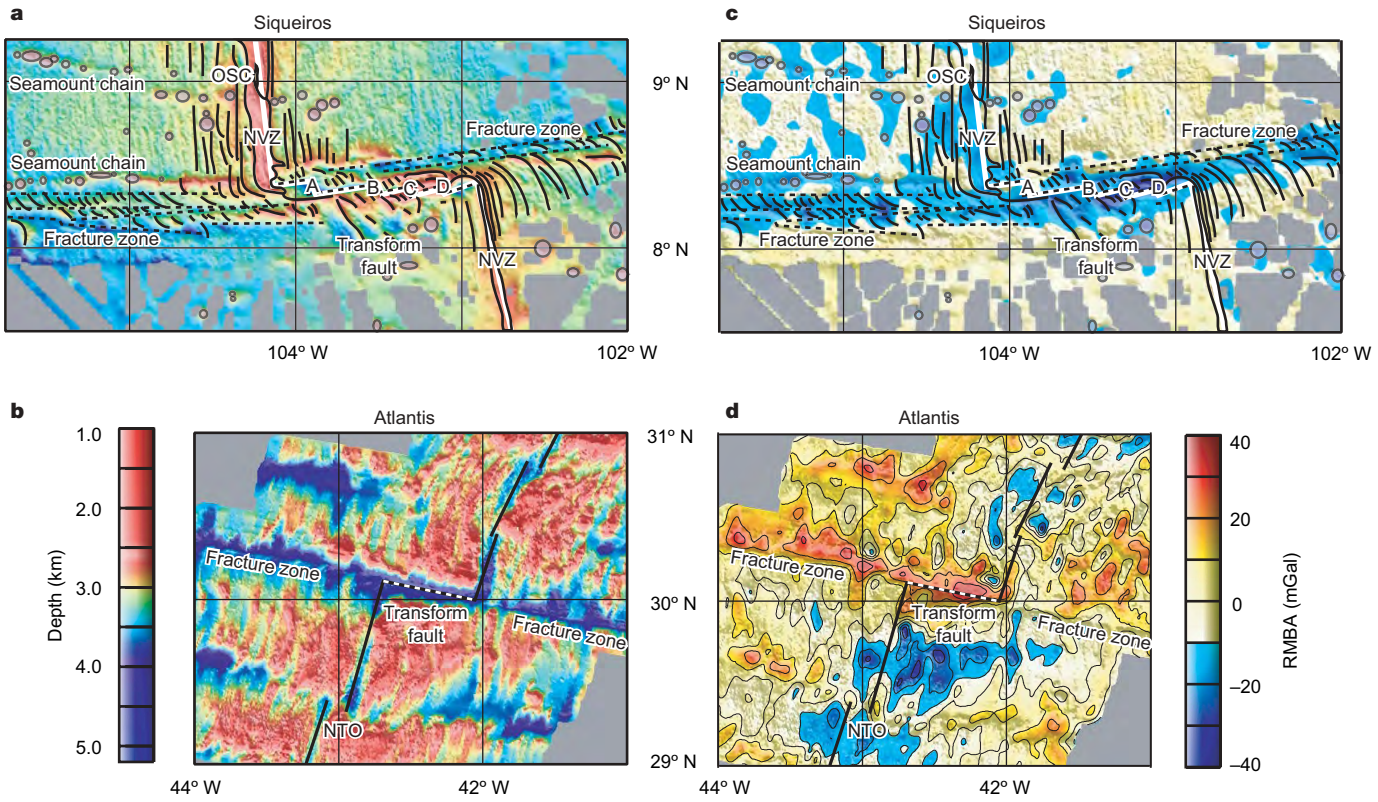

Figure 1 | Comparison of bathymetry and RMBA of the Siqueiros transform on the East Pacific Rise and Atlantis transform on the Mid-Atlantic Ridge, at the same map scale. **a**, Bathymetric map for the Siqueiros transform with geologic interpretation[16]. Solid black lines indicate the seafloor fabric, circles show locations of seamounts, and dashed black lines show the locations of the fracture zones and transform fault. The solid white line indicates the location of the plate boundary used in the 3D thermal model. ITSCs are labelled A, B, C and D[16]. NVZ, neo-volcanic zone; OSC, overlapping spreading centre. **b**, Bathymetric map for the Atlantis transform. The solid black line indicates location of the plate boundary used in the 3D thermal model, and the dashed portion indicates the Atlantis transform fault. **c**, Calculated RMBA map for the Siqueiros transform fault with geologic interpretation overlaid from **a**. **d**, Calculated RMBA map for the Atlantis transform fault. Seabeam bathymetry compiled by the RIDGE multibeam synthesis project (http://ocean-ridge.ldeo.columbia.edu/general/html/home.html).

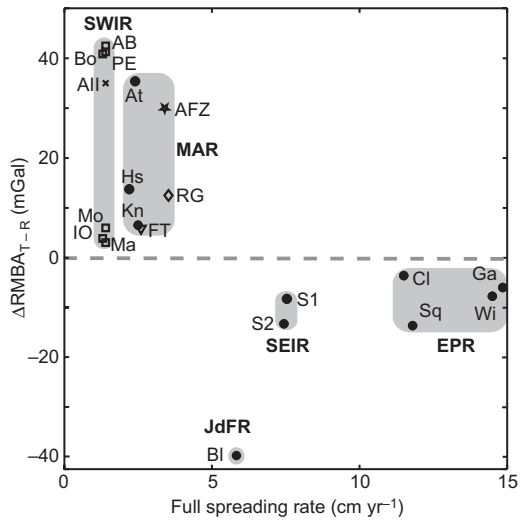

Figure 2 | Compilation of $\Delta RMBA_{T-R}$ values for the 19 transform systems analysed. The new RMBA calculations from this study are marked with solid circles. Previous RMBA studies are indicated by the open symbols: square[29], triangle[12], cross[30], star[11], diamond[3]. Abbreviations for ridges: SWIR, Southwest Indian Ridge; MAR, Mid-Atlantic Ridge; JdFR, Juan de Fuca Ridge; SEIR, Southeast Indian Ridge; EPR, East Pacific Rise. Abbreviations for transform faults: Bo, Bouvet; IO, Islas Orcadas; AB, Andrew Bain; PE, Prince Edward; AII, Atlantis II; Mo, Moshesh; Ma, Marion; At, Atlantis; Hs, Hayes; Kn, Kane; FT, Fifteen-Twenty; AFZ, Ascension; RG, Rio Grande; Bl, Blanco; S2, SEIR2; S1, SEIR1; Cl, Clipperton; Sq, Siqueiros; Wi, Wilkes; Ga, Garrett.

decrease in seismic velocities of ~1 km s^{-1} in the Clipperton transform fault[18] can be explained by porosity increases in the range of 1–5.5% for crack aspect ratios of 0.01–0.1 (ref. 19). Calculations in Fig. 3 demonstrate that an average porosity increase of 2–7% within the upper crust down to the brittle-ductile transition (600 °C) is required to produce the negative $\Delta RMBA_{T-R}$ values of up to −14 mGal observed at fast-slipping transforms (Fig. 2). However,

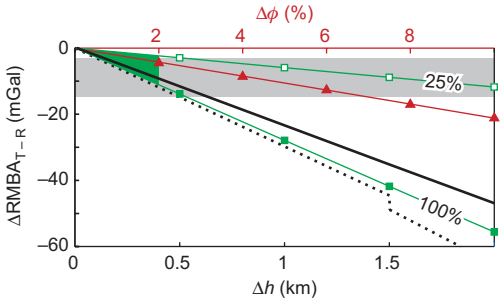

Figure 3 | Results of 2D forward models showing the predicted $\Delta RMBA_{T-R}$. Data are shown as a function of increase in crustal thickness through layer 2A (dotted black line) or overall crustal thickening (solid black line); increases in porosity (Φ, red line); or the presence of serpentinized mantle (green lines indicate percentage; green shading indicates serpentine stability field). Δh indicates change in layer thickness. Grey shading indicates the observed $\Delta RMBA_{T-R}$ at fast-slipping transforms. The kink in the curve for increase in layer 2A corresponds to thickening of layer 2A beyond the thickness of layer 2B in the reference model. See Supplementary Fig. 7 for model details.

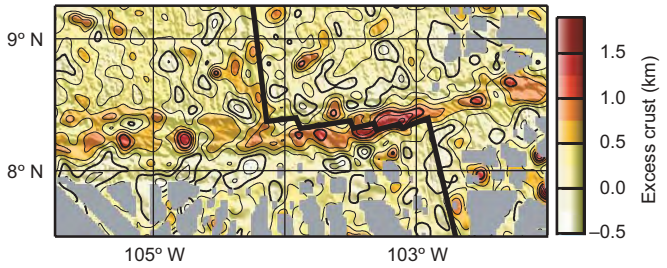

Figure 4 | Lateral variations in crustal thickness required to explain the observed RMBA in the Siqueiros transform system (Fig. 1c). Excess crust is defined as the deviation from the reference crustal thickness of 6 km, assuming sea water, crust and mantle densities of 1,030, 2,730 and 3,300 kg m^{-3}, respectively.

an increase in porosity in excess of 5% at slow-slipping transforms will negate the effect of crustal thinning and result in negative $\Delta RMBA_{T-R}$ (Supplementary Fig. 7). Consequently, a porosity increase of 2–5% is consistent with observed $\Delta RMBA_{T-R}$ and seismic data at both slow- and fast-slipping transform faults.

Serpentinization of mantle peridotite can also generate negative $\Delta RMBA_{T-R}$. However, the calculated 500 °C isotherm, which represents the upper limit of serpentine stability[20], is located within the crust at all fast-slipping transform faults considered in this study (see Methods) and therefore predicts no mantle serpentinization. Invoking hydrothermal cooling (see Supplementary Methods) depresses the 500 °C isotherm to an average depth of 6.4 km at Siqueiros transform fault. Assuming 100% serpentinization (density of 2,550 kg m^{-3}) of the mantle where temperatures are <500 °C results in a negative $\Delta RMBA_{T-R}$ of 0 to -10 mGal, which is slightly less than the values of up to -14 mGal observed at fast-slipping transform faults (Fig. 3). However, if 100% serpentinization were pervasive above the 500 °C isotherm at slow-slipping transform faults, it would negate the effects of crustal thinning and produce negative $\Delta RMBA_{T-R} < -100$ mGal (Supplementary Fig. 7g). Therefore, although low degrees of mantle serpentinization might contribute to the observed negative RMBA along fast-slipping transform faults, current thermal models for oceanic transform faults make it unlikely that serpentinization alone can explain the systematic differences between fast- and slow-slipping transforms.

Finally, we estimate the magnitude of variations in crustal thickness required to explain the RMBA observed along the Siqueiros transform by inverting the observed RMBA relative to a reference model with average crustal density of 2,730 kg m^{-3} (ref. 1) (Fig. 4). Along the eastern domain of Siqueiros transform, we predict an excess crustal thickness of >1.5 km, while in the western domain of the transform and in the off-axis fracture zones excess crust ranges from 0.5–1.5 km. The $\Delta RMBA_{T-R}$ observed at fast-slipping transform faults can also be produced by increasing layer 2A by 0.25–0.6 km (Fig. 3).

Although increased rock porosity and mantle serpentinization could both contribute to the observed negative RMBA along intermediate- and fast-slipping transform faults, we believe that local crustal thickening is probably the dominant mechanism. Areas of localized deformation, such as fault zones, are expected to exhibit enhanced cracking and alteration. However, the most negative RMBA values observed at intermediate- and fast-slipping transform faults correspond to bathymetric highs flanking the transforms instead of the transform troughs where deformation is likely to be localized. Local excess crust within intermediate- and fast-slipping transform fault domains may result from a combination of magmatic accretion mechanisms including: (1) lateral transport of excess magma from the ridge axis into the transform fault domain[16,21]; (2) magmatic accretion at intra-transform spreading centres[16,22]; (3) the pooling of lava within topographic lows[23]; and/or (4) 'leaky' magmatic accretion along the entire transform fault[24].

Lateral dyke propagation from a central magma chamber has been proposed to explain crustal thickness variations along slow-spreading ridge segments[25]. At magmatically robust segments along intermediate and fast-spreading ridges, a continuous magma chamber may exist beneath the entire segment and feed dykes from the ridge transform intersection into the transform fault domain. A possible geologic expression of this mechanism is overshooting ridge tips, which are common bathymetric features of robust ridge segments at intermediate- and fast-spreading ridge transform intersections[16] (see Supplementary Figs 2–5). Bathymetry and RMBA of overshooting ridge tips at intermediate and fast-spreading ridges suggest that dykes propagating along the ridge axis penetrate past the transform fault into juxtaposed old oceanic crust, curve in the direction of the transform, and locally increase the crustal thickness of an already full-thickness crust (Fig. 5b). Geologic evidence from the northwestern segment of Blanco transform indicates significant

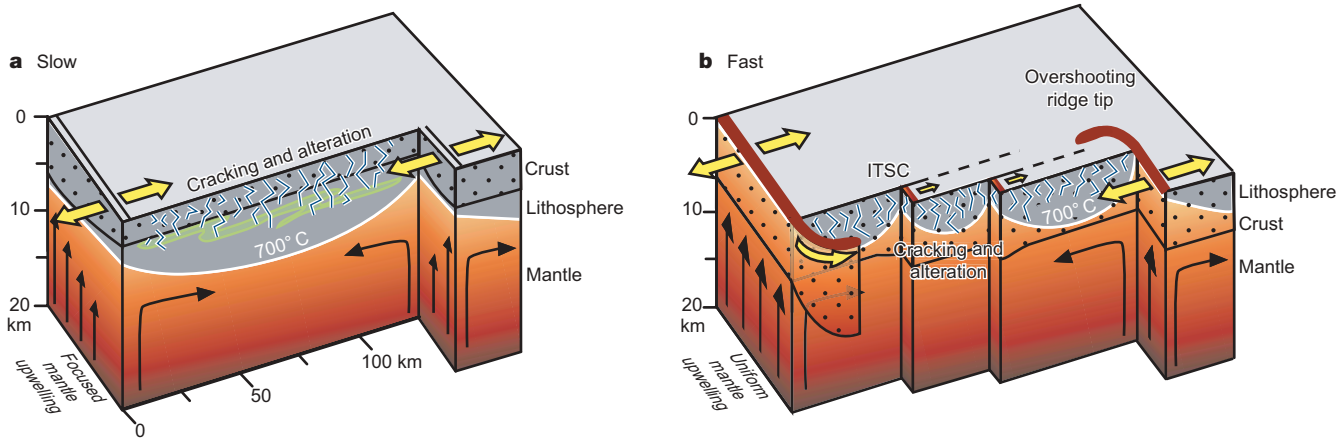

Figure 5 | A spreading-rate-dependent model of crustal accretion and mantle upwelling based on observed RMBA calculations and morphological features at transform fault systems on slow- and fast-spreading ridges. Large yellow arrows indicate plate motion vectors; smaller black arrows indicate mantle flow. The grey area with white outline represents the lithosphere as defined by the 700 °C isotherm, while the crust is identified by dotted pattern. The blue cracks and the green wiggles indicate regions of increased porosity and serpentinization, respectively. **a**, Slow-spreading ridges exhibit focused mantle upwelling at segment centres and crustal thinning towards segment ends and transform faults. **b**, Fast-spreading ridges have relatively uniform mantle upwelling. The negative $\Delta RMBA_{T-R}$ at fast-spreading ridges may result from: (1) excess magma supply on ridge segments causing over-shooting ridges and dyke injection into the transform fault domain; (2) increased porosity within the transform; (3) actively accreting ITSCs; (4) pooling of extruded lavas within the transform fault.

increases in the extrusive lava layer with a possible overshooting ridge tip source[21]. However, for this model to explain the RMBA along the entire transform fault (rather than just in the fracture zone), transform-parallel dyke propagation must extend at least half the distance between ridge transform intersections (~50–75 km). Bathymetric data demonstrate that overshooting ridge tips wrap around and into transform faults, but the cause of this curvature is unclear. Possible explanations include response to the local stress field at the ridge transform intersection, and/or dyke propagation along preferential pathways created by pre-existing transform-parallel cracks.

Fast-slipping transform faults typically contain multiple fault segments separated by intra-transform spreading centres (ITSC)[13,26]. Several ITSCs at East Pacific Rise transform faults have been sampled and contain fresh basaltic lavas indicating crustal accretion within the transform fault domain[16,22]. In some cases, such as the Garrett transform fault (Supplementary Fig. 2), the ITSCs occur in pull-apart basins and do not appear to increase the crustal thickness. Alternatively, along the eastern portion of Siqueiros transform (Fig. 1a) ITSCs are associated with negative RMBA. Thus, ITSCs may thicken crust in some localities.

A third possible mechanism for local crustal thickening is the pooling of erupted lavas in topographic lows within the transform fault domain[23] (Fig. 5b). However, the majority of the negative RMBA values we have observed correspond with topographic highs, indicating that this might not be a dominant mechanism. Finally, because off-axis melt is considered abundant at fast-spreading ridges[27], 'leaky' magmatic accretion might occur along the entire length of some transform faults[24]. This mechanism could cause increases in crustal thickness and may be enhanced by transtensional forces acting upon a transform fault owing to plate motion reorganizations[24].

Thus the observed negative RMBA values at intermediate- and fast-slipping transform faults may be the result of a combination of mechanisms, including increases in rock porosity, mantle serpentinization and/or crustal thickening. Further detailed constraints are required to distinguish among the potential contributors to the observed gravity anomalies. However, the strong correlation of the negative RMBA with topographic highs flanking the transforms suggests crustal thickening as a potentially important mechanism for at least some of the observed negative RMBA values. Systematic occurrence of crustal thickening, if confirmed, would require a modification of our current understanding of how three-dimensional magma accretion occurs along intermediate- and fast-spreading ridges in the vicinity of transform fault discontinuities.

METHODS SUMMARY

The mantle Bouguer anomaly was calculated following the method of ref. 1. This technique removes the effect of seafloor topography and 6 km of reference crust from the satellite free air gravity[28]. The RMBA was calculated by removing from the mantle Bouguer anomaly the effects of lithospheric cooling as estimated from a three-dimensional (3D) passive mantle upwelling model calculated using the commercial finite-element modelling software package COMSOL MULTIPHYSICS 3.2 (for model details see Supplementary Tables 1 and 2). The RMBA reflects the deviation of sub-seafloor density structure from the reference model described in Supplementary Table 2. When constructing the thermal models for segmented transform faults, we incorporated the best-known geometry of transform fault segments and assumed steady-state crustal accretion at the ITSCs.

We define $\Delta RMBA_{T-R} = [(RMBA_T - RMBA_{R1}) + (RMBA_T - RMBA_{R2})]/2$, where $RMBA_{R1}$ and $RMBA_{R2}$ are the average RMBA values on the adjacent ridge segments 1 and 2, respectively, and $RMBA_T$ is the average RMBA value along the transform fault domain (see Supplementary Fig. 8). Where digital data are available[12,29], $RMBA_{R1}$ and $RMBA_{R2}$ were calculated by averaging the values at the centre of each adjacent ridge segment within a 20-km-wide and 50-km-long box. At the East Pacific Rise, Juan de Fuca Ridge, and Southeast Indian Ridge, where the transform fault zones are wider owing to segmentation, $RMBA_T$ was calculated by averaging over a 20-km-wide swath centred 20 km from the ridge transform intersections. At the Mid-Atlantic Ridge and Southwest Indian Ridge the RMBA values were averaged over a 10-km-wide swath centred 20 km from the ridge transform intersections. Where digital data are unavailable[3,11,30], average values were estimated from published profiles and maps of the transform faults and their adjacent ridge segments.

Full Methods and any associated references are available in the online version of the paper at www.nature.com/nature.

Received 22 September 2006; accepted 24 May 2007.

1. Kuo, B. Y. & Forsyth, D. W. Gravity anomalies of the ridge transform intersection system in the South Atlantic between 31 and 34.5°S: Upwelling centers and variations in crustal thickness. *Mar. Geophys. Res.* **10,** 205–232 (1988).
2. Lin, J., Purdy, G. M., Schouten, H., Sempere, J.-C. & Zervas, C. Evidence from gravity data for focused magmatic accretion along the Mid-Atlantic Ridge. *Nature* **344,** 627–632 (1990).
3. Blackman, D. K. & Forsyth, D. W. Isostatic compensation of tectonic features of the Mid-Atlantic Ridge: 25°-27°30'S. *J. Geophys. Res.* **96,** 11741–11758 (1991).
4. Lin, J. & Phipps Morgan, J. The spreading rate dependence of three-dimensional mid-ocean ridge gravity structure. *Geophys. Res. Lett.* **19,** 13–16 (1992).
5. Tolstoy, M., Harding, A. & Orcutt, J. Crustal thickness on the Mid-Atlantic Ridge: bulls-eye gravity anomalies and focused accretion. *Science* **262,** 726–729 (1993).
6. Detrick, R. S., Needham, H. D. & Renard, V. Gravity-anomalies and crustal thickness variations along the Mid-Atlantic Ridge between 33°N and 40°N. *J. Geophys. Res.* **100,** 3767–3787 (1995).
7. Escartin, J. & Lin, J. Ridge offsets, normal faulting, and gravity anomalies of slow spreading ridges. *J. Geophys. Res.* **100,** 6163–6177 (1995).
8. Minshull, T. A. Along-axis variations in oceanic crustal density and their contribution to gravity anomalies at slow-spreading ridges. *Geophys. Res. Lett.* **23,** 849–852 (1996).
9. Canales, J. P., Detrick, R. S., Lin, J., Collins, J. A. & Toomey, D. R. Crustal and upper mantle seismic structure beneath the rift mountains and across a nontransform offset at the Mid-Atlantic Ridge (35°N). *J. Geophys. Res.* **105,** 2699–2719 (2000).
10. Hooft, E. E. E., Detrick, R. S., Toomey, D. R., Collins, J. A. & Lin, J. Crustal thickness and structure along three contrasting spreading segments of the Mid-Atlantic Ridge, 33.5°-35°N. *J. Geophys. Res.* **105,** 8205–8226 (2000).
11. Bruguier, N. J., Minshull, T. A. & Brozena, J. M. Morphology and tectonics of the Mid-Atlantic Ridge, 7°-12°S. *J. Geophys. Res.* **108,** 2093, doi:10.1029/2001JB001172 (2003).
12. Fujiwara, T. *et al.* Crustal evolution of the Mid-Atlantic Ridge near the Fifteen-Twenty Fracture Zone in the last 5 Ma. *Geochem. Geophys. Geosyst.* **4,** 1024, doi:10.1029/2002GC000364 (2003).
13. Fox, P. J. & Gallo, D. G. A tectonic model for ridge-transform-ridge plate boundaries: Implications for the structure of oceanic lithosphere. *Tectonophysics* **104,** 205–242 (1984).
14. Macdonald, K. C. *et al.* A new view of the mid-ocean ridge from the behavior of ridge-axis discontinuities. *Nature* **335,** 217–225 (1988).
15. Canales, J. P., Detrick, R., Toomey, D. R. & Wilcock, S. D. Segment-scale variations in the crustal structure of 150–300 kyr old fast spreading oceanic crust (East Pacific Rise, 8°15'N-10°5'N) from wide-angle seismic refraction profiles. *Geophys. J. Int.* **152,** 766–794 (2003).
16. Fornari, D. J. *et al.* Structure and topography of the Siqueiros transform-fault system—Evidence for the development of intra-transform spreading centers. *Mar. Geophys. Res.* **11,** 263–299 (1989).
17. Blackman, D. K., Cann, J. R., Janssen, B. & Smith, D. K. Origin of extensional core complexes: Evidence from the Mid-Atlantic Ridge at Atlantis Fracture Zone. *J. Geophys. Res.* **103,** 21315–21333 (1998).
18. Van Avendonk, H. J. A., Harding, A. J., Orcutt, J. A. & McClain, J. S. Contrast in crustal structure across the Clipperton transform fault from travel time tomography. *J. Geophys. Res.* **106,** 10961–10981 (2001).
19. Wilkens, R. H., Fryer, G. J. & Karsten, J. Evolution of porosity and seismic structure of upper oceanic-crust—Importance of aspect ratios. *J. Geophys. Res.* **96,** 17981–17995 (1991).
20. Ulmer, P. & Trommsdorff, V. Serpentine stability to mantle depths and subduction-related magmatism. *Science* **268,** 858–861 (1995).
21. Karson, J. A., Tivey, M. A. & Delaney, J. R. Internal structure of uppermost oceanic crust along the Western Blanco Transform Scarp: Implications for subaxial accretion and deformation at the Juan de Fuca Ridge. *J. Geophys. Res.* **107,** 2181, doi:10.1029/2000JB000051 (2002).
22. Perfit, M. R. *et al.* Recent volcanism in the Siqueiros transform fault: Picritic basalts and implications for MORB magma genesis. *Earth Planet. Sci. Lett.* **141,** 91–108 (1996).
23. Begnaud, M. L., McClain, J. S., Barth, G. A., Orcutt, J. A. & Harding, A. J. Velocity structure from forward modeling of the eastern ridge-transform intersection area of the Clipperton Fracture Zone, East Pacific Rise. *J. Geophys. Res.* **102,** 7803–7820 (1997).
24. Menard, H. W. & Atwater, T. Origin of fracture zone topography. *Nature* **222,** 1037–1040 (1969).
25. Fialko, Y. A. & Rubin, A. M. Thermodynamics of lateral dike propagation: Implications for crustal accretion at slow spreading mid-ocean ridges. *J. Geophys. Res.* **103,** 2501–2514 (1998).

26. Gregg, P. M., Lin, J. & Smith, D. K. Segmentation of transform systems on the East Pacific Rise: Implications for earthquake processes at fast-slipping oceanic transform faults. *Geology* **34,** 289–292 (2006).
27. Sohn, R. A. & Sims, K. W. W. Bending as a mechanism for triggering off-axis volcanism on the East Pacific Rise. *Geology* **33,** 93–96 (2005).
28. Smith, W. H. F. & Sandwell, D. T. Global seafloor topography from satellite altimetry and ship depth soundings. *Science* **277,** 1957–1962 (1997).
29. Georgen, J. E., Lin, J. & Dick, H. J. B. Evidence from gravity anomalies for interactions of the Marion and Bouvet hotspots with the Southwest Indian Ridge: Effects of transform offsets. *Earth Planet. Sci. Lett.* **187,** 283–300 (2001).
30. Muller, M. R., Minshull, T. A. & White, R. S. Crustal structure of the Southwest Indian Ridge at the Atlantis II Fracture Zone. *J. Geophys. Res.* **105,** 25809–25828 (2000).

Supplementary Information is linked to the online version of the paper at www.nature.com/nature.

Acknowledgements This work was supported by a National Science Foundation (NSF) Graduate Research Fellowship (P.M.G.), the NSF (M.D.B.), and the Woods Hole Oceanographic Institution Deep Ocean Exploration Institute (J.L. and L.G.J.M.). We are grateful for discussions with J. P. Canales, A. Cruse, H. J. B. Dick, D. Fornari, D. Forsyth, J. Georgen, J. Gregg, T. Grove, G. Hirth, D. Lizarralde, J. McGuire, M. Perfit, H. Schouten, D. Smith and the WHOI geophysics group. This manuscript was greatly improved by a review by R. Buck.

Author Information Reprints and permissions information is available at www.nature.com/reprints. The authors declare no competing financial interests. Correspondence and requests for materials should be addressed to P.G. (pgregg@whoi.edu).

METHODS

Because there is an inherent non-uniqueness in gravity calculations, we have created several 2D forward models[31] to quantify the effects of various mechanisms on the gravity signature of a ridge–transform system (Supplementary Fig. 7). The light blue and orange shaded regions in Supplementary Fig. 7 indicate the extent of $\Delta RMBA_{T-R}$ observed along transform faults at slow- and fast-spreading ridges, respectively. The density used for each of the layers is indicated in Supplementary Fig. 7. These values do vary in nature[32–35].

In the first suite of models we varied the crustal thickness by Δh either entirely as a change of layer 2A, layer 2B, or proportionally throughout the entire crust (Supplementary Figs 7a, b and c, respectively). All three mechanisms act to decrease $\Delta RMBA_{T-R}$ within the range of fast-slipping transforms with <1 km of excess material. Increasing layer 2A requires the least amount of excess material with 0.25–0.6 km. The kink in model A results from increasing layer 2A beyond the thickness of layer 2B.

The second suite of models considers increased porosity in the brittle layer (temperatures $<600\,^{\circ}C$). Two 3D thermal models were calculated to obtain the average depth to the 600 °C isotherm along the Siqueiros transform fault: (1) the initial 3D passive mantle upwelling model, outlined in the Methods (the red dashed line at ~3 km depth on Supplementary Figs 7d and e), and (2) a hydrothermally cooled model in which heat conductivity is increased tenfold to 4 km depth (the blue dashed line at 6.4 km depth on Supplementary Figs 7d and e). Density changes due to variations in porosity are defined as: $\rho(\Phi) = (1-\Phi)\rho_{rock} + \Phi\rho_{sw}$, where Φ is the porosity, ρ_{rock} is the density of the host rock, and ρ_{sw} is the density of sea water. Assuming that the brittle–ductile transition is at ~3 km, porosity would need to be increased 2–7% to achieve the $\Delta RMBA_{T-R}$ values of magnitude −14 mGal observed at fast-slipping transform faults.

Similar calculations were performed for slow-slipping transforms, assuming a thicker brittle layer, as was calculated for the Atlantis transform fault. These results indicate that it is difficult to explain the $\Delta RMBA_{T-R}$ at both fast and slow-slipping transforms simultaneously, assuming similar porosity structures in both regions. Because it is unlikely that there will be large increases in porosity down to 9 km depth at slow-slipping transform faults, even though it is within the pressure constraints suggested by ref. 36, we have rerun the 2D slow-slipping transform model with increased porosity to 6 km depth. While porosity increases in excess of 8% still act to negate the effect of crustal thinning at slow-slipping transform faults, moderate increases of 2–5% are consistent with $\Delta RMBA_{T-R}$ values at both slow- and fast-slipping transform faults (Supplementary Fig. 7e).

The final set of forward models includes serpentinization of the mantle beneath the transform fault (Supplementary Figs 7f and g). As in the porosity models, we have incorporated two 3D thermal calculations at the Siqueiros transform to obtain average depths to the 500 °C isotherm, which limits the serpentine stability field[20] to 2.5 km for uncooled and 6.4 km for hydrothermally cooled lithosphere. Without hydrothermal cooling the 500 °C isotherm lies well within the upper crust and there is no predicted mantle serpentinization. However, if hydrothermal cooling is applied from 0 to 4 km depth, an end member model of 100% serpentinization will result in a $\Delta RMBA_{T-R}$ of −10 mGal, which is the average of the observed $\Delta RMBA_{T-R}$ for fast-slipping transform faults. If a similar model for mantle serpentinization is applied at a slow-slipping transform fault, mantle serpentinization down to the hydrothermally cooled 500 °C isotherm would produce such a large negative RMBA that it would completely offset the effect of crustal thinning, which is inconsistent with observations.

Additionally, we calculated a modified RMBA at the Siqueiros transform using the hydrothermally cooled thermal model and the density for 100% serpentine (2,550 kg m^{-3}) in all regions of the mantle (>6 km depth) where the temperature is $<500\,^{\circ}C$. Even though this correction maximizes the effect of serpentine, it decreases the average $\Delta RMBA_{T-R}$ within the Siqueiros transform fault domain by only <2 mGal, and reduces the calculated excess crustal thickness by <200 m.

Laboratory experiments suggest that, if the crust is thinned and mantle upwelling occurs, hydrothermal fluid penetration through thermal cracking and grain boundary wetting will reach only ~4–6 km depth[37]. Therefore, it is unlikely that hydrothermal fluids will penetrate to great enough depths to serpentinize large regions of mantle beneath fast-slipping transform faults. Moreover, depressing the 500 °C isotherm through hydrothermal cooling is inconsistent with calculated earthquake depths at oceanic transform faults[38]. On the other hand, slow-slipping transform faults display significant crustal thinning and are cooler than intermediate- and fast-slipping transform faults, implying that a larger portion of the underlying mantle resides in the serpentine stability field. However, the locally positive RMBA observed at slow-slipping transform faults reflects crustal thinning despite the potential for significant serpentinized peridotite[9]. Together, these results indicate that, while mantle serpentinization may occur at intermediate and fast-slipping transform faults, the direct contribution of serpentinization to the gravity signature is likely to be negligible.

31. Blakely, R. J. *Potential Theory in Gravity and Magnetic Applications* 378 (Cambridge Univ. Press, New York, 1996).
32. Cochran, J. R., Fornari, D. J., Coakley, B. J., Herr, R. & Tivey, M. A. Continuous near-bottom gravity measurements made with a BGM-3 gravimeter in DSV Alvin on the East Pacific Rise crest near 9° 31′ N and 9° 50′ N. *J. Geophys. Res.* **104,** 10841–10861 (1999).
33. Stevenson, J. M., Hildebrand, J. A., Zumberge, M. A. & Fox, C. G. An ocean-bottom gravity study of the southern Juan-De-Fuca Ridge. *J. Geophys. Res.* **99,** 4875–4888 (1994).
34. Johnson, H. P., Pruis, M. J., Van Patten, D. & Tivey, M. A. Density and porosity of the upper oceanic crust from seafloor gravity measurements. *Geophys. Res. Lett.* **27,** 1053–1056 (2000).
35. Escartin, J., Hirth, G. & Evans, B. Nondilatant brittle deformation of serpentinites: Implications for Mohr-Coulomb theory and the strength of faults. *J. Geophys. Res.* **102,** 2897–2914 (1997).
36. Behn, M. D. & Kelemen, P. B. Relationship between seismic P-wave velocity and the composition of anhydrous igneous and meta-igneous rocks. *Geochem. Geophys. Geosyst.* **4,** 1041, doi:10.1029/2002GC000393 (2003).
37. deMartin, B., Hirth, G. & Evans, B. in *Mid-Ocean Ridges: Hydrothermal Interactions Between Lithosphere and Oceans* (eds German, C. R., Lin, J. & Parsons, L. M.) 318 (American Geophysical Union, Washington DC, 2004).
38. Abercrombie, R. E. & Ekstrom, G. Earthquake slip on oceanic transform faults. *Nature* **410,** 74–77 (2001).

Spreading rate dependence of gravity anomalies along oceanic transform faults

Patricia M. Gregg[1], Jian Lin[2], Mark D. Behn[2], and Laurent G.J. Montési[2]

[1] *Dept. of Geology and Geophysics, MIT/WHOI Joint Program, Woods Hole, Massachusetts 02543, USA*

[2] *Dept. of Geology and Geophysics, Woods Hole Oceanographic Institution, Woods Hole, Massachusetts 02543, USA*

S1. Supplementary Figures

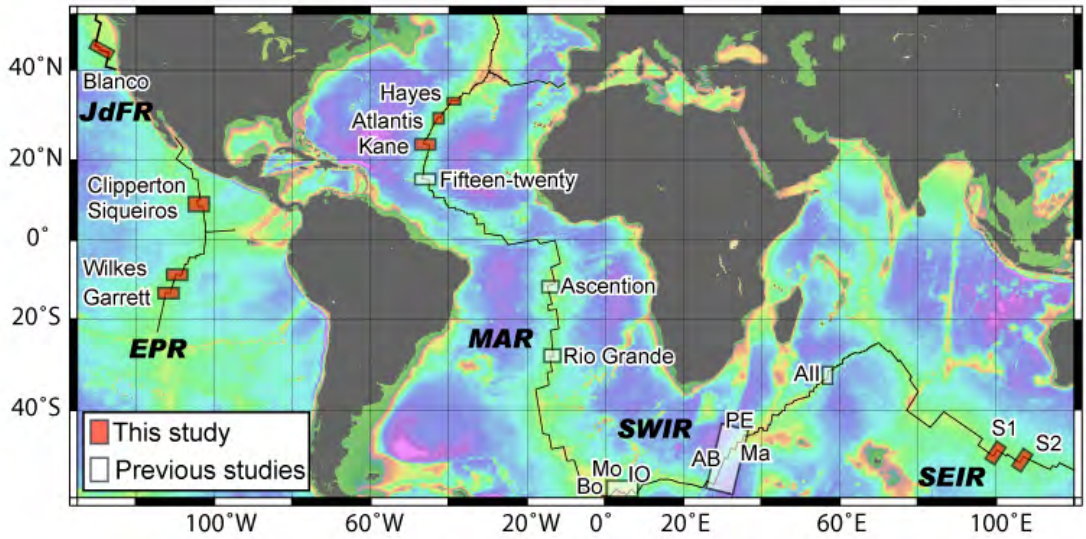

Supplementary Figure 1. Bathymetric map indicating the location of the 19 transform faults analyzed. Thin black lines show the location of plate boundaries for the areas of interest. New residual mantle Bouguer anomaly (RMBA) calculations have been performed for transform faults in orange boxes (presented in Supplemental Figs. 2-5). Regions where RMBA calculations have been previously published[1-5] are indicated by transform faults in white boxes. We included previous RMBA studies only if both transform fault and corresponding ridges were analyzed by the same authors using the same parameters. All other RMBA studies we considered from slow-spreading ridges implied $\Delta RMBA_{T-R} > 0$. MAR – Mid Atlantic Ridge, EPR – East Pacific Rise, JdFR – Juan de Fuca Ridge, SWIR – Southwest Indian Ridge, SEIR – Southeast Indian Ridge, AB – Andrew Bain FZ, Bo – Bouvet FZ, Mo – Moshesh FZ, PE – Prince Edward FZ, AII – Atlantis II FZ, IO – Islas Orcadas FZ, Ma – Marion FZ, S1 – SEIR1, S2 – SEIR2.

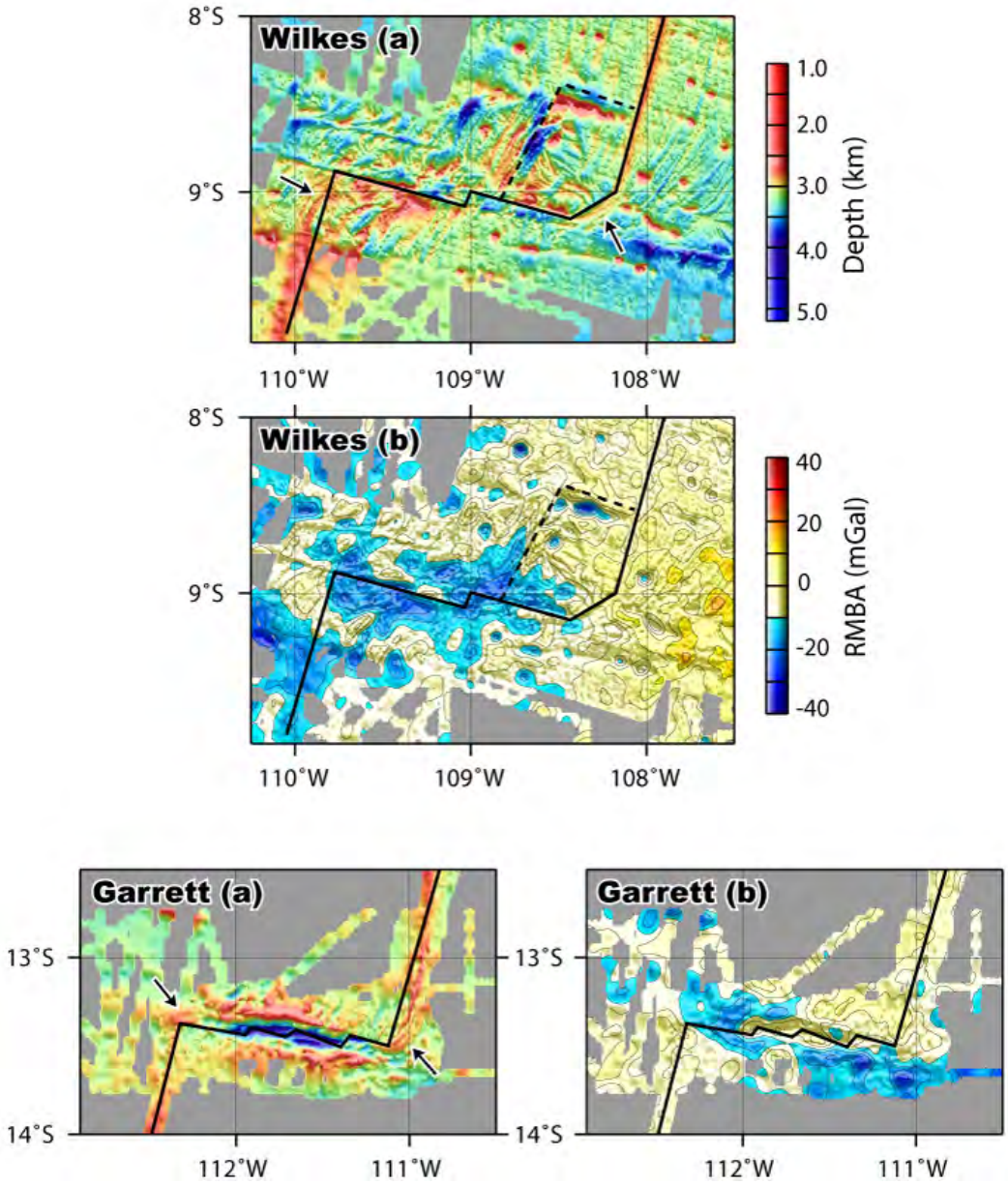

Supplementary Figure 2. a) Seafloor depth and (b) RMBA for the Wilkes and Garrett transform faults on the East Pacific Rise. The solid black line indicates the plate boundary used for 3D thermal models at each region[6,7]. Arrows specify the location of overshooting ridge tips (ORTs) at ridge transform intersections (RTI). The dotted line outlines the Wilkes nanoplate[6]. All supplemental maps (Supplemental Figs 2-6) are at the same map scale.

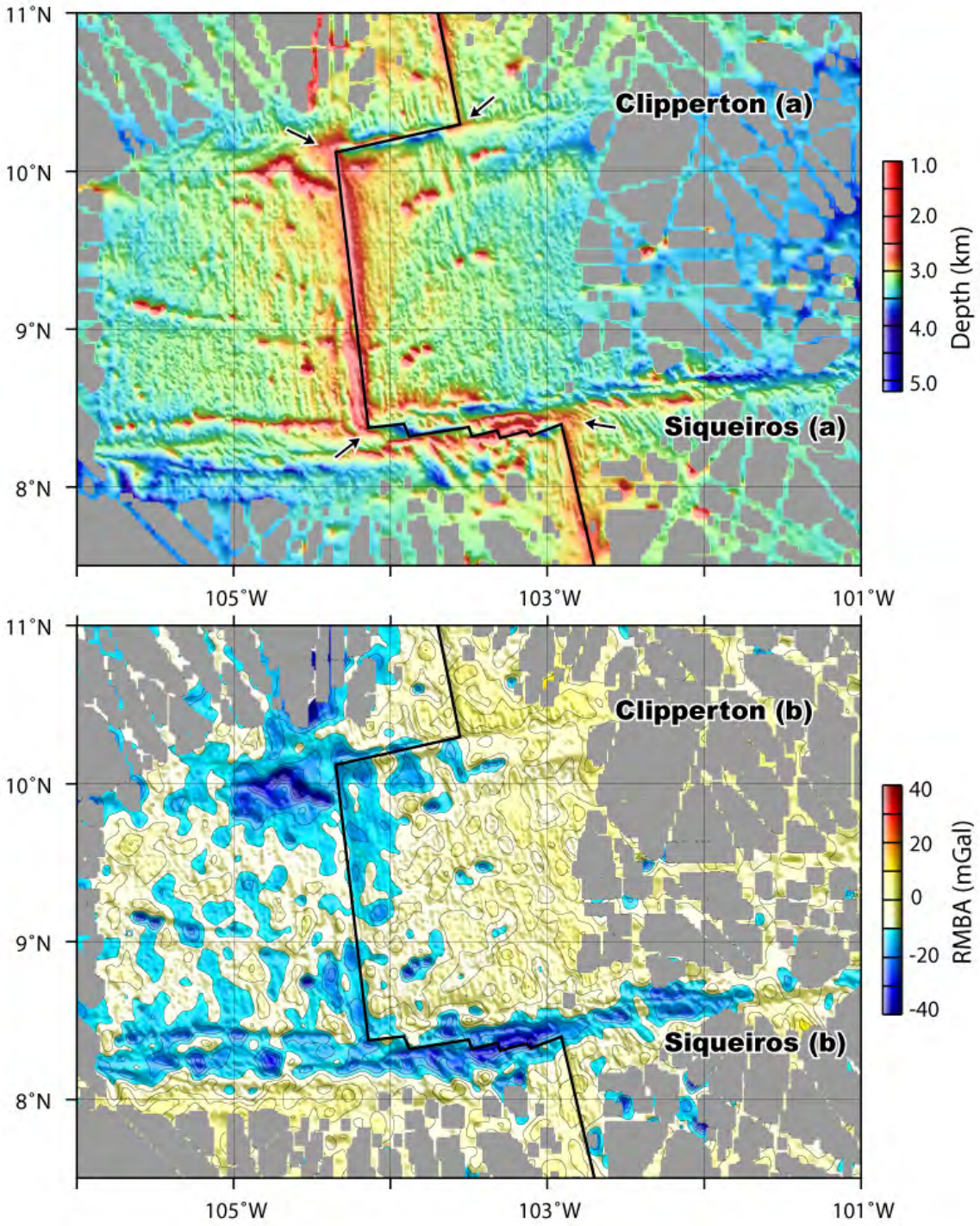

Supplementary Figure 3. a) Seafloor depth and b) RMBA for the Siqueiros and Clipperton transform faults on the EPR. The solid black line indicates the plate boundary used for the 3D thermal models, and black arrows indicate location of ORTs[8]. Note the Clipperton seamount chain to the south and west of the western RTI.

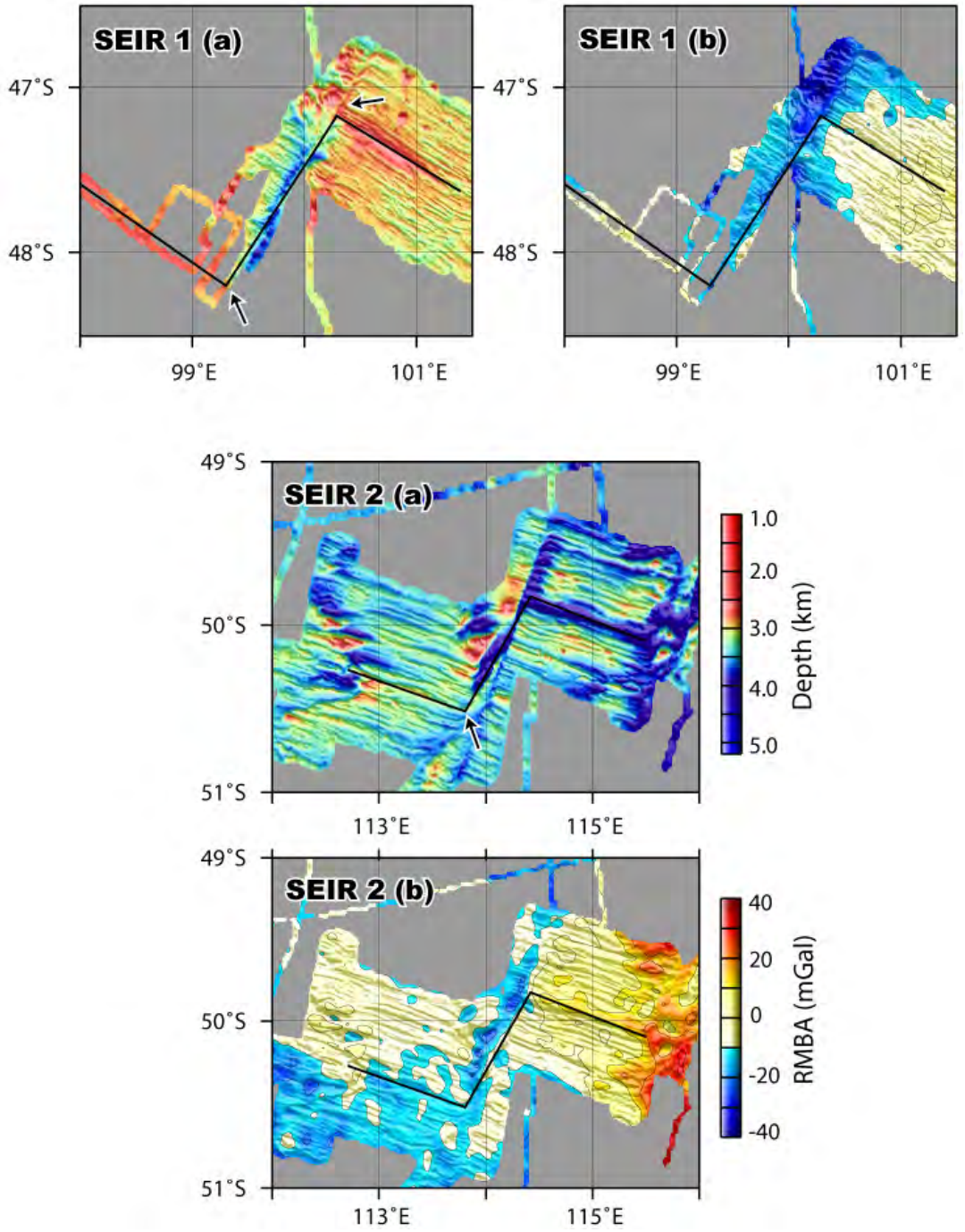

Supplementary Figure 4. a) Seafloor depth and (b) RMBA for Southeast Indian Ridge transform 1 and transform 2. The solid black line indicates the plate boundary used for 3D thermal models at each region[9,10], and black arrows indicate ORTs.

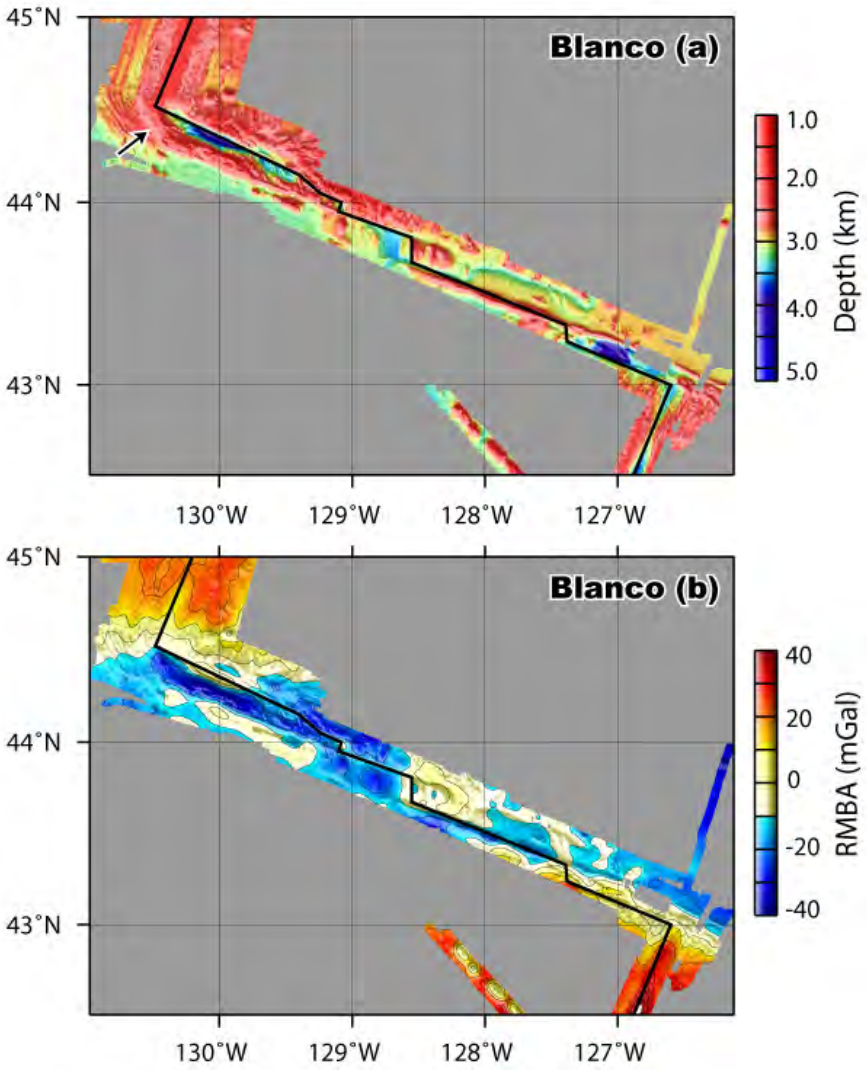

Supplementary Figure 5. a) Seafloor depth and (b) RMBA for the Blanco transform fault on the Juan de Fuca Ridge. The solid black line indicates the plate boundary used for 3D thermal models at each region[11]. The Blanco transform fault is the most anomalous of the $\Delta RMBA_{T\text{-}R}$ calculated (main text Fig. 2). There are several complications in this region, which are not incorporated into the 3D thermal model, including the close proximity to the Cascadia subduction zone as well as a proposed serpentine intrusion forming Blanco Ridge along the southeastern portion of the transform fault (~128°W, 43.5°N)[11,12]. While a serpentine block has been proposed along the southeastern portion of the transform, the most negative RMBA values are associated with overshooting ridge tip and bathymetric highs along the northwestern portion of the transform fault (~130°W, 44.25°N), and are likely due to crustal increases. Karson et al. (2002)[13] note that the extrusive volcanic layer along the northwestern portion of Blanco is substantially thicker than what is predicted by seismic studies in this region. An increase in layer 2A agrees with our observation of negative RMBA along this portion of the Blanco transform.

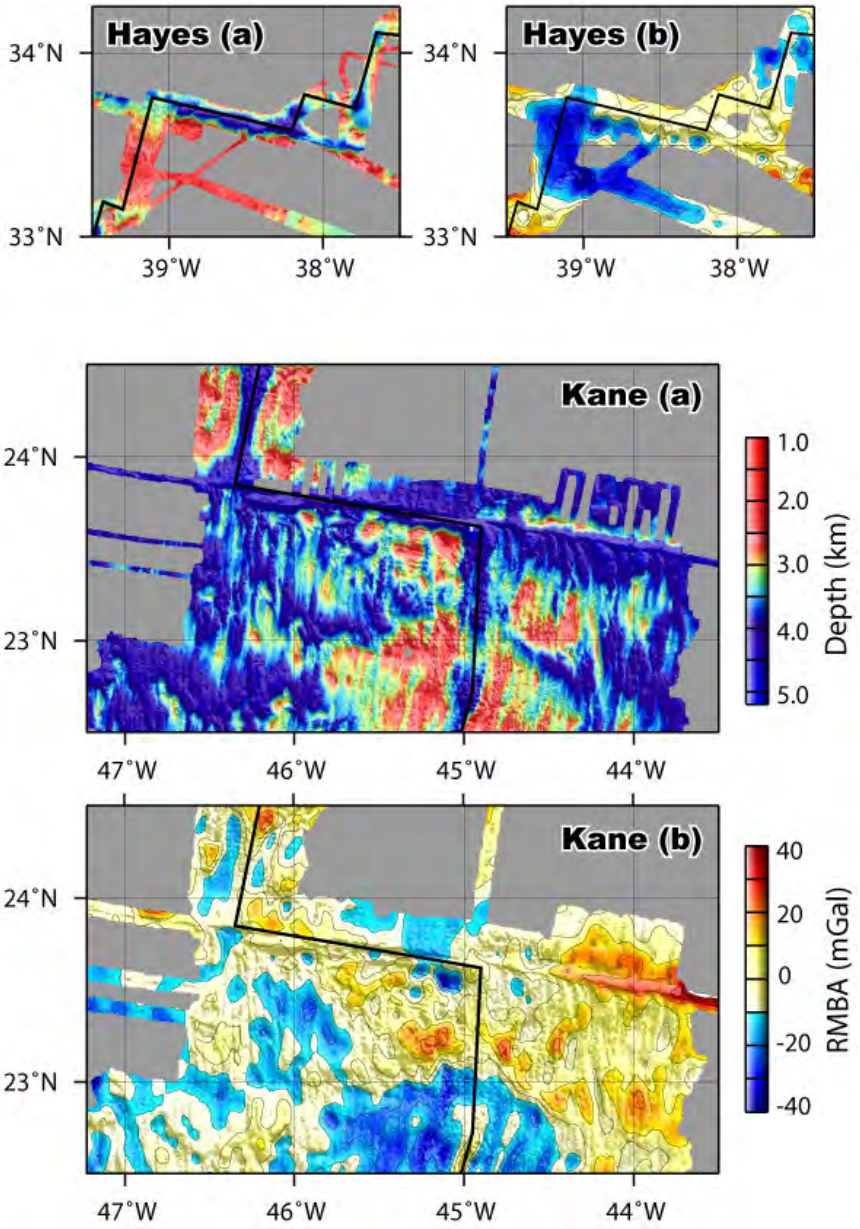

Supplementary Figure 6. a) Seafloor depth and (b) RMBA for the Hayes and Kane transform faults on the Mid-Atlantic Ridge. Clear RMBA "bulls-eye" minima are observed at segment centers, in agreement with previous studies at slow-spreading mid-ocean ridges.

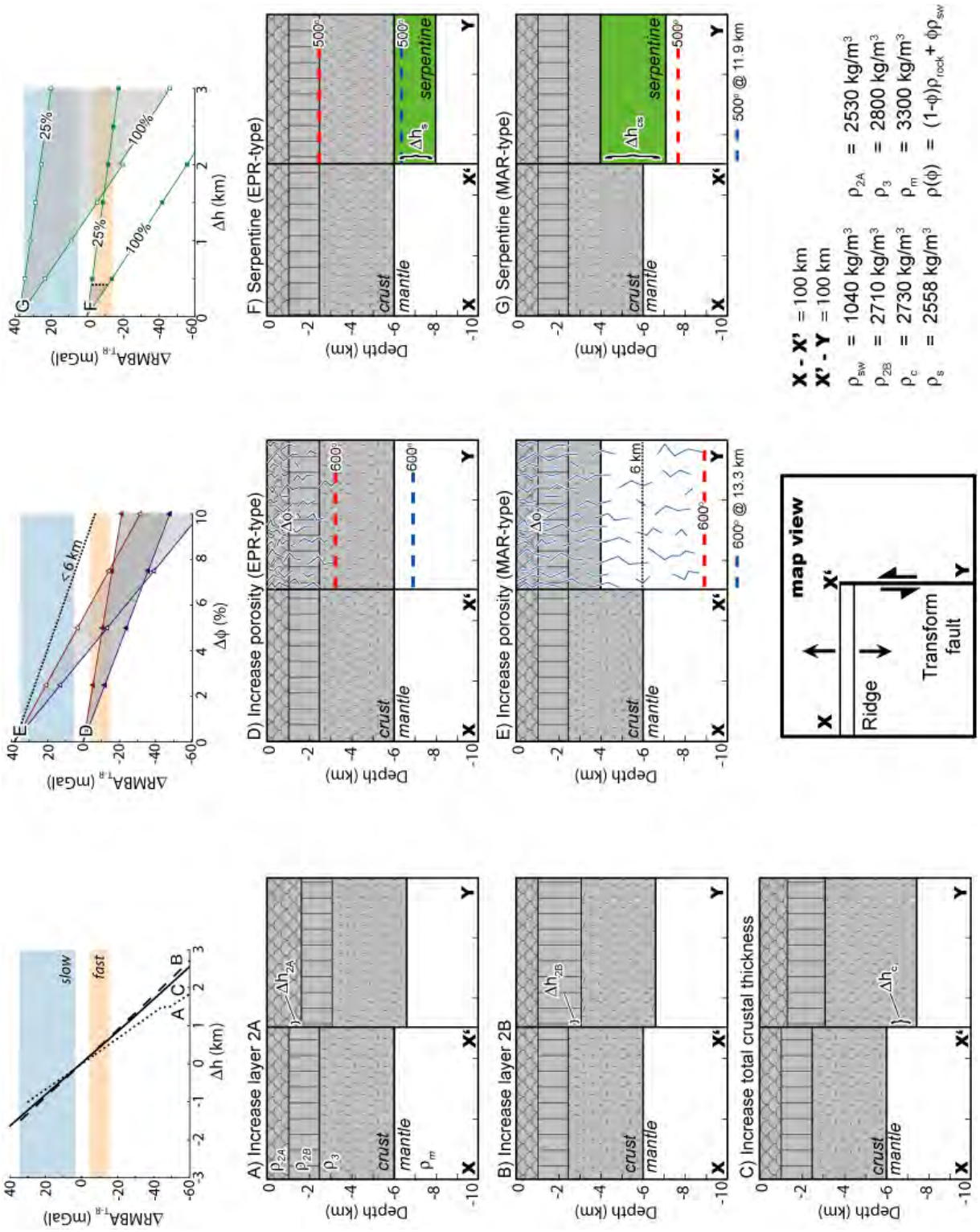

Supplementary Figure 7. Three suites of forward models. The calculated $\Delta RMBA_{T-R}$ are plotted on the top panels. The light blue and orange shaded region indicates the extent of $\Delta RMBA_{T-R}$ observed at slow and fast-slipping transform faults, respectively. A) Change in layer 2A thickness (dotted line), B) Change in layer 2B thickness (dashed line), C) Proportional change in crustal thickness (solid black line). D)

Porosity increase in the brittle layer at an EPR-type fast-spreading ridge-transform system. The model illustration demonstrates that porosity is increased down to the brittle-ductile transition, the 600°C isotherm, for both an un-cooled (red dashed line) and hydrothermally cooled (blue dashed line) thermal model. The red line with solid red triangles indicates un-cooled 600°C isotherm and blue line with solid blue triangles indicates hydrothermally cooled 600°C isotherm in the model results. E) Porosity increase in the brittle layer at a MAR-type slow-spreading ridge-transform system. The red line with open triangles indicates un-cooled 600°C isotherm and blue line with open triangles indicates hydrothermally cooled 600°C isotherm. Black dashed line indicates the effect of increasing porosity only to 6 km depth. F) Serpentinization of the mantle at an EPR-type system (green line with solid green squares). 100% and 25% serpentinization is shown, and the shaded region marks the serpentine stability field for the hydrothermally cooled ridge-transform system. The model illustration demonstrates that extent of serpentine stability, the 500°C isotherm, for both an un-cooled (red dashed line) and hydrothermally cooled (blue dashed line) thermal model. The depth of the 500°C isotherm represents the average depth calculated by the 3D thermal model within the Siqueiros transform. G) Serpentinization of the mantle at an MAR-type system (green line with open squares). The kinks visible in the 100% and to a lesser extent the 25% curve result when the thickness of the serpentine layer exceeds 6 km depth, the replacement thickness of layer 3.

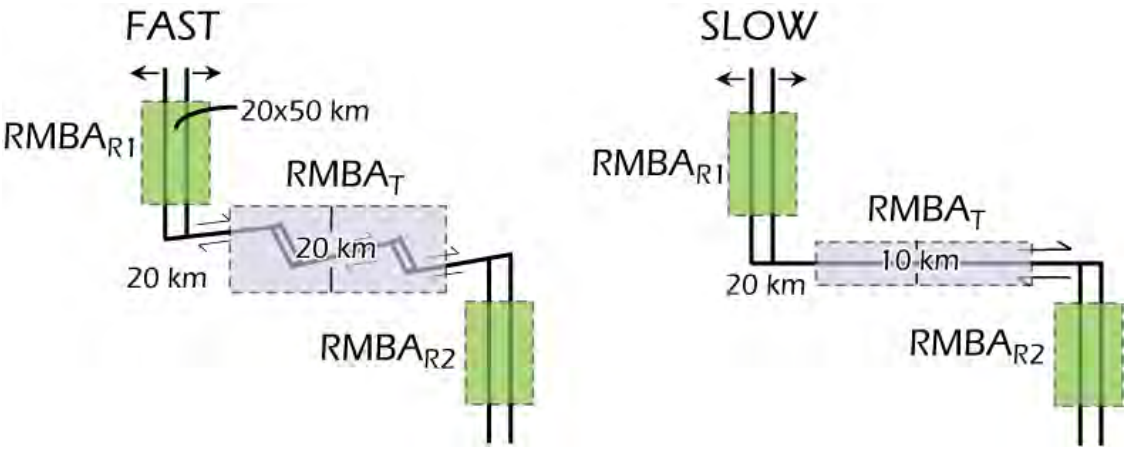

Supplementary Figure 8. A schematic of the calculation of $\Delta RMBA_{T-R}$. $\Delta RMBA_{T-R} = [(RMBA_T - RMBA_{R1}) + (RMBA_T - RMBA_{R2})]/2$, where $RMBA_{R1}$ and $RMBA_{R2}$ are the average RMBA values on the adjacent ridge segments 1 and 2, respectively, and $RMBA_T$ is the average RMBA value along the transform fault domain. The ridge RMBA values, $RMBA_{R1}$ and $RMBA_{R2}$, were calculated by averaging the values at the centre of each adjacent ridge segment within a 20 km-wide and 50 km-long box shown by green boxes. At the East Pacific Rise, Juan de Fuca Ridge, and Southeast Indian Ridge, where the transform fault zones are wider due to segmentation, $RMBA_T$ was calculated by averaging over a 20 km-wide swath centred 20 km from the RTIs, indicated by the blue boxes. At the Mid-Atlantic Ridge and Southwest Indian Ridge the RMBA values were averaged over a 10 km-wide swath centred 20 km from the RTIs. This convention is also used in determining $\Delta RMBA_{T-R}$ for the 2D models.

S2. Supplementary Tables

Supplementary Table 1. Transform fault characteristics[6-11,14,15].

Transform fault	Ridge System	Appx. Latitude	Full-slip rate (cm/yr)	Length (km)	No. of Segments	$\Delta RMBA_{T-R}$ (mGals)
Garrett*	EPR	12°S	14.9	130	4	-6.0
Wilkes	EPR	8°S	14.5	100	3	-7.7
Siqueiros	EPR	8°N	11.8	150	5	-13.6
Clipperton	EPR	10°N	11.5	90	1	-3.6
SEIR 1	SEIR	48°S	7.54	135	1	-8.2
SEIR 2	SEIR	50°S	7.44	80	1	-13.2
Blanco	JdFR	42°N	5.8	350	5	-39.7
Kane	MAR	24°N	2.5	160	1	6.6
Atlantis	MAR	30°N	2.4	70	1	35.4
Hayes	MAR	34°N	2.2	90	1	13.7

* Asymmetry of slip at Garrett transform[14] has been incorporated in the thermal model of Garrett transform fault.

Supplemental Table 2. Parameters used in RMBA calculation.

Parameter	Value
Sea water density, kg m^{-3}	1,030
Reference crustal density, kg m^{-3}	2,730
Reference mantle density, kg m^{-3}	3,300
Serpentine density (100% serpentinization), kg m^{-3}	2,550
Reference crustal thickness, km	6
Thermal boundary layer thickness, km	100
Asthenospheric temperature, °C	1,350
Thermal diffusivity, m^2s^{-1}	10^{-6}
Coefficient of thermal expansion, $°C^{-1}$	2.4×10^{-5}

Supplementary References

1. Blackman, D. K. & Forsyth, D. W. Isostatic compensation of tectonic features of the Mid-Atlantic Ridge - 25°-27°30's. *J. Geophys. Res.* **96**, 11741-11758 (1991).
2. Bruguier, N. J., Minshull, T. A. & Brozena, J. M. Morphology and tectonics of the Mid-Atlantic Ridge, 7°-12°S. *J. Geophys. Res.* **108**, 2093, doi:10.1029/2001JB001172 (2003).
3. Fujiwara, T. et al. Crustal evolution of the Mid-Atlantic Ridge near the Fifteen-Twenty Fracture Zone in the last 5 Ma. *Geochem. Geophys. Geosyst.* **4**, 1024, doi:10.1029/2002GC000364 (2003).
4. Georgen, J. E., Lin, J. & Dick, H. J. B. Evidence from gravity anomalies for interactions of the Marion and Bouvet hotspots with the Southwest Indian Ridge: Effects of transform offsets. *Earth Planet. Sci. Lett.* **187**, 283-300 (2001).

5. Muller, M. R., Minshull, T. A. & White, R. S. Crustal structure of the Southwest Indian Ridge at the Atlantis II Fracture Zone. *J. Geophys. Res.* **105**, 25809-25828 (2000).
6. Goff, J. A., Fornari, D. J., Cochran, J. R., Keeley, C. & Malinverno, A. Wilkes transform system and nannoplate. *Geology* **21**, 623-626 (1993).
7. Hekinian, R., Bideau, D., Cannat, M., Francheteau, J. & Hebert, R. Volcanic activity and crust mantle exposure in the ultrafast Garrett transform-fault near 13°28'S in the Pacific. *Earth Planet. Sci. Lett.* **108**, 259-275 (1992).
8. Fornari, D. J. et al. Structure and topography of the Siqueiros transform-fault system - Evidence for the development of intra-transform spreading centers. *Mar. Geophys. Res.* **11**, 263-299 (1989).
9. Cochran, J. R., Fornari, D. J., Coakley, B. J., Herr, R. & Tivey, M. A. Continuous near-bottom gravity measurements made with a BGM-3 gravimeter in DSV Alvin on the East Pacific Rise crest near 9 degrees 31 ' N and 9 degrees 50 ' N. **104**, 10841-10861 (1999).
10. West, B. P. & Sempere, J. C. Gravity anomalies, flexure of axial lithosphere, and along-axis asthenospheric flow beneath the southeast Indian ridge. *Earth Planet. Sci. Lett.* **156**, 253-266 (1998).
11. Dziak, R. P. et al. Recent tectonics of the Blanco Ridge, eastern blanco transform fault zone. *Mar. Geophys. Res.* **21**, 423-450 (2000).
12. Bonatti, E. Vertical tectonism in oceanic fracture zones. *Earth Planet. Sci. Lett.* **37**, 369-379 (1978).
13. Karson, J. A., Tivey, M. A. & Delaney, J. R. Internal structure of uppermost oceanic crust along the Western Blanco Transform Scarp: Implications for subaxial accretion and deformation at the Juan de Fuca Ridge. *J. Geophys. Res.* **107**, 2181, doi:10.1029/2000JB000051 (2002).
14. Conder, J. A., Forsyth, D. & Parmentier, E. M. Asthenospheric flow and asymetry of the East Pacific Rise, MELT area. *J. Geophys. Res.* **107**, 2344, doi:10.1029/2001JB000807 (2002).
15. Lin, J., Purdy, G. M., Schouten, H., Sempere, J.-C. & Zervas, C. Evidence from gravity data for focused magmatic accretion along the Mid-Atlantic Ridge. *Nature* **344**, 627-632 (1990).